Available online at www.sciencedirect.com
ScienceDirect
Electrochimica Acta 52 (2007) 7936–7945
ELECTROCHIMICA Acta
www.elsevier.com/locate/electacta

Pore-network modeling of liquid water transport in gas diffusion layer of a polymer electrolyte fuel cell

Puneet K. Sinha, Chao-Yang Wang *

Electrochemical Engine Center (ECEC), Department of Mechanical and Nuclear Engineering, The Pennsylvania State University, University Park, PA 16802, United States

Received 16 April 2007; received in revised form 14 June 2007; accepted 21 June 2007
Available online 27 June 2007

Abstract

A pore-network model is developed to study the liquid water movement and flooding in a gas diffusion layer (GDL), with the GDL morphology taken into account. The dynamics of liquid water transport at the pore-scale and evolution of saturation profile in a GDL under realistic fuel cell operating conditions is examined for the first time. It is found that capillary forces control liquid water transport in the GDL and that liquid water moves in connected clusters with finger-like liquid waterfronts, rendering concave-shaped saturation profiles characteristic of fractal capillary fingering. The effect of liquid coverage at the GDL–channel interface on the liquid water transport inside GDL is also studied, and it is found that liquid coverage at the GDL–channel interface results in pressure buildup inside the GDL causing the liquid water to break out from preferential locations.

Keywords: Liquid water transport; Gas diffusion layer; Pore-network modeling; Capillary fingering; Surface coverage

1. Introduction

Automotive, stationary and portable applications place an ever-increasing demand for fuel cell technologies with high performance, low cost, and extended durability. Among them, the polymer electrolyte fuel cell (PEFC) has emerged as the most promising power source for a broad range of applications. Despite tremendous recent progress in overall cell performance, a pivotal performance/durability limitation in PEFCs centers on liquid water transport and resulting flooding in the constituent components. Liquid water blocks reactant transport through the gas diffusion layer (GDL), and incurs mass transport losses by hindering oxygen transport to the active reaction sites in the catalyst layer (CL). Therefore, a detailed understanding of liquid water transport in the GDL is necessary to facilitate development of techniques and GDL materials to mitigate flooding and associated mass transport losses. While considerable research, both numerical and experimental [1–3] has been conducted to address liquid water transport in a GDL and its effect on PEFC performance, the present understanding is still incomplete to address the following basic questions:

1. What is the liquid water transport mechanism through a fibrous GDL structure? How do GDL microstructure and wetting characteristics influence the liquid water transport?
2. What are the mechanisms and influences of GDL–channel interfacial coverage on flooding dynamics in a GDL?

Existing theoretical models follow the macroscopic approach based on two-phase Darcy's law to investigate liquid water transport in PEFC. These models cannot incorporate the GDL morphology and require material-specific capillary pressure–liquid saturation and relative permeability–liquid saturation relationships. Investigation of these constitutive relations for PEFC-specific materials is scarce in literature. Recently, Gostick et al. [4] measured capillary pressure as a function of liquid saturation for different GDL materials in ex situ experiments using the method of standard porosimetry (MSP) and octane–air system. Using the octane–air system that completely wets GDL as required by MSP remains to be justified for measuring capillary pressure between water and air in hydrophobic GDL. Neither in situ measurements of the capillary pressure

* Corresponding author. Tel.: +1 814 863 4762; fax: +1 814 863 4848.
E-mail address: cxw31@psu.edu (C.-Y. Wang).

0013-4686/$ – see front matter © 2007 Elsevier Ltd. All rights reserved.
doi:10.1016/j.electacta.2007.06.061

nor any experimental measurements of relative permeability for a PEFC GDL have been reported in the open literature.

Existing experimental efforts based on neutron radiography (NR) and magnetic resonance imaging (MRI), owing to their low spatial resolution (∼25 μm), 2D nature, and magnetic field sensitivity to carbon, have not been able to yield data of the liquid water distribution in a fuel cell GDL [5]. Most recently, Djilali and co-workers [6,7] investigated the evolution of gas–liquid interface inside a GDL using fluorescence microscopy. However, these ex situ experiments, where liquid water injection rate was 0.02 ml/min over an active area of 0.0314 cm^2 and hence corresponded to a current density of 112 A cm^{-2}, do not reflect realistic PEFC operating conditions. Specifically, in any ex situ experiment, capillary number, defined as the ratio of viscous and capillary forces, and viscosity ratio, defined as the ratio of viscosities of invading and defending fluids, must be matched with that found in an operating fuel cell as these are fundamental parameters determining mechanisms of liquid water transport in GDL. The importance of these parameters in the delineation of liquid water transport in a GDL will be further elaborated in a later section.

Therefore, in order to resolve the open questions regarding liquid water transport in a GDL, pore-scale studies taking GDL microstructure and wetting characteristics into account are warranted. Pore-scale models can be broadly divided into pore-network (PN) models, lattice-gas (LG), lattice-Boltzmann (LB) models, and molecular dynamic (MD) models. The pore-network modeling approach, being less computationally intensive while accounting for all the relevant two-phase flow physics, is ideally suited to investigate liquid water transport in a GDL. More discussions on various pore-scale modeling approaches can be found in Ref. [8]. In PN modeling, a porous medium is represented at the microscopic scale by a lattice of wide pores connected by narrower constrictions called throats. PN modeling started with the pioneering work of Fatt [9–11] who computed capillary pressure and relative permeability in a network of interconnected pores. Since then, network models have become more sophisticated both in terms of reconstructing a physically realistic and topologically equivalent pore-network structure and incorporating detailed flow dynamics in porous media [12,13]. Various researchers have predicted and experimentally validated capillary pressure and relative permeabilities for a range of soils and rocks with PN models and further investigated the effects of heterogeneity, mixed-wettability [14,15], viscosity ratios and injection rates [16] on relative permeability. In addition, the PN models have been applied to investigate dynamics of multiphase flow [17] and drying in porous media [18]. In recent years, Nam and Kaviany [19] and Schulz et al. [20] implemented pore-scale modeling approaches to compute effective diffusivity and capillary pressure as a function of liquid water saturation for a carbon paper GDL, respectively. However, no attempt has been made to elucidate liquid water transport in a GDL at the pore-level.

The objective of this study is to develop a basic understanding of liquid water transport in a hydrophobic carbon paper GDL under realistic PEFC operating conditions, and of how the GDL microstructure affects the movement of liquid water. The paper is organized as follows: First, the fundamental parameters governing liquid water transport at the pore-level are discussed. Then, a physically realistic pore-network structure for a hydrophobic carbon paper GDL is described and algorithms to simulate two-phase flow in the pore-network are presented. Finally, the dynamics of liquid water transport in a hydrophobic GDL is described and the effect of GDL–channel interfacial coverage is discussed. The effect of capillary number (i.e. liquid water flow rate) on liquid saturation profile is presented and the need to carry out ex situ experiments under realistic fuel cell operating conditions is stressed.

2. Liquid water transport in porous media

Two-phase flow in porous media is governed by capillary and viscous forces, and their relative magnitude governs the two-phase distribution and flow regimes. Two-phase flow is designated as a drainage process if the invading fluid is non-wetting and an imbibition process otherwise. Liquid water transport in a hydrophobic GDL is thus essentially a drainage process. Lenormand et al. [21] proposed a phase diagram, illustrated in Fig. 1, to describe displacement of a wetting phase by a non-wetting phase in the absence of buoyancy forces. They found that immiscible displacement is governed by capillary number, *Ca*, and viscosity ratio, *M*, defined as

$$\mathrm{Ca} = \frac{u\mu_{\mathrm{nw}}}{\sigma} \qquad M = \frac{\mu_{\mathrm{nw}}}{\mu_{\mathrm{wet}}} \tag{1}$$

where subscripts 'nw' and 'wet' stand for the non-wetting and wetting phase, respectively. u is the velocity of non-wetting phase and σ is the surface tension. Fig. 1 also shows characteristic distributions of the non-wetting phase in a two-dimensional cross-section for all the three flow regimes [21–23]. For a typical fuel cell application, the viscosity ratio is 17.5 and capillary number is of the order of 10^{-8}; therefore, two-phase flow in a GDL falls in the regime of capillary fingering. For a detailed description of capillary fingering, readers may refer to Ref. [22].

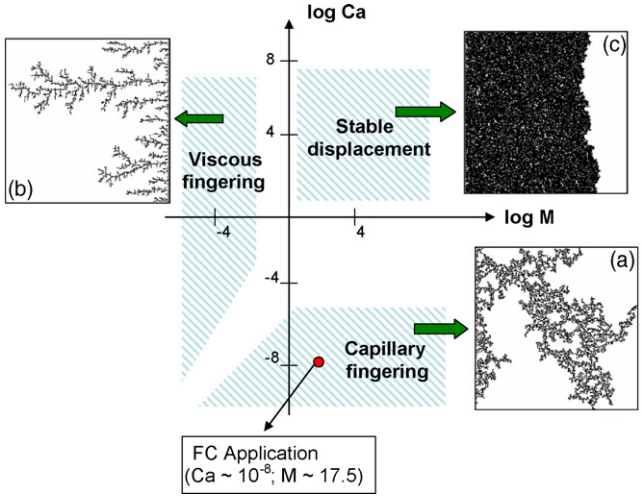

Fig. 1. Schematic representation of phase diagram showing various flow regimes and characteristic distributions of non-wetting phase for these regimes [21–23].

3. Pore-network model

3.1. Pore-network structure

In a classical pore-network modeling framework, a porous medium is discretized in a network of wide pore spaces, which are connected by narrower regions called throats. The morphology of a real porous medium is incorporated in the network structure using pore and throat size distributions and their connectivity. Over the years, extensive efforts were made to reconstruct a topologically equivalent skeleton to describe the network for a real porous medium. Several approaches to represent a real porous medium via network of pores are summarized as follows:

1. Generation of random pore-network structure, calibrated with known physical properties of the real porous media.
2. Reconstruction of three-dimensional network from the images of two-dimensional sections. The porosity and two-point correlation functions can be measured from these sections and used to generate three-dimensional network with the same statistical properties.
3. Reconstruction of pore network from the three-dimensional image of pore space obtained from e.g. X-ray micro-tomography at resolutions around 1 μm.
4. Reconstruction of porous media by modeling the processes by which it is made.

An overview of these approaches with their limitations and advantages was given by Blunt et al. [12]. Randomly distributed fibers in the carbon paper GDL furnish highly disordered pore space topology; therefore, a high resolution three-dimensional image would be required to construct a topologically equivalent pore-network structure. As a first attempt, however, the methodology of Nam and Kaviany [19] is followed in which carbon paper is regarded to consist of randomly stacked regular fiber screens that renders a three-dimensional random tetragonal pore-network structure with pores cubic in shape and throats of square cross-section, as depicted in Fig. 2. In the present study, pore and throat radii are assumed to have a cut-off log normal distribution. Pore and throat radii are defined as the radii of the largest sphere that can be inscribed in a pore and a throat, respectively. In addition, a throat length is defined to characterize the throats in the network. For throat connecting pores i and j, the throat length is given by

$$l_{i,j} = L - (r_i + r_j) \tag{2}$$

where L is the distance between two adjacent pores and assumed to be constant in the present work.

The geometric and transport parameters used in the present PN model are summarized in Table 1. The absolute parameters of the present pore-network structure are summarized and compared with Toray® carbon paper parameters in Table 2. Recently, Gostick et al. [24] reported significant anisotropy in permeability for various carbon paper GDLs, with highly aligned-fiber materials showing a maximum anisotropy factor of 2. Further research to incorporate permeability anisotropy in an equivalent pore-network structure for a carbon paper GDL is currently underway.

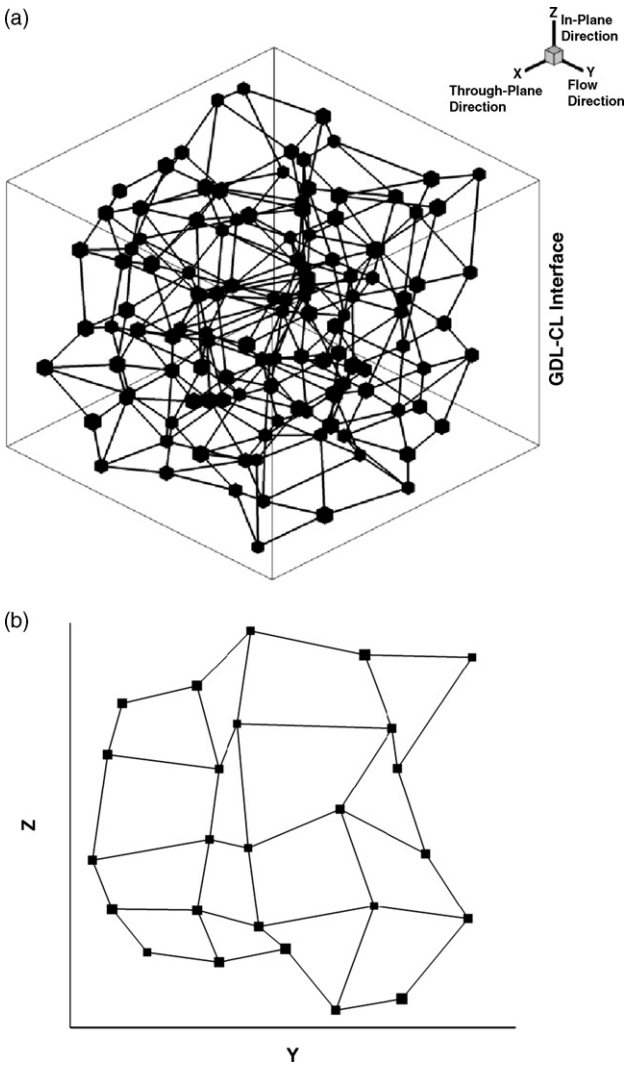

Fig. 2. Schematic of pore-network model for a carbon paper GDL: (a) 3D view and (b) 2D cross-section showing the connectivity of pores in a plane.

3.2. Model assumptions

The model assumptions are as follows:

1. Wetting properties are assumed to be constant in the network.
2. While the radius of a throat serves to define its hydraulic conductance, the volume contributed by the throats is assumed to be small relative to the pore volumes.
3. Only one fluid can reside in a throat.
4. Flow within a throat is assumed to be laminar and given by Hagen–Poiseuille law.
5. The resistance offered by a pore to flow is assumed to be negligible.
6. Fluids are assumed to be incompressible.

Table 1
Pore-network and transport parameters

Parameter	Value
Network parameters	
Mean pore radius, r_{mean}	10 μm
Minimum pore radius, r_{min}	9 μm
Maximum pore radius, r_{max}	12.5 μm
Mean throat radius, $r_{th,mean}$	6 μm
Minimum throat radius, $r_{th,min}$	4 μm
Maximum throat radius, $r_{th,max}$	8.5 μm
L	25 μm
Number of pores in x-direction	11
Number of pores in y-direction	30
Number of pores in z-direction	30
Cut-off log-normal distribution: for pore and throat size distribution	$f(r,\sigma_{nd}) = \frac{\sqrt{2}\exp[-0.5(\ln(r/r_{mean})/\sigma_{nd})^2]}{\sqrt{\pi\sigma_{nd}^2}r[\mathrm{erf}(\ln(r_{max}/r_{mean})/\sqrt{2\sigma_{nd}^2})-\mathrm{erf}(\ln(r_{min}/r_{mean})/\sqrt{2\sigma_{nd}^2})]}$
Standard deviation in pore and throat size distribution, σ_{nd}	1.0
Transport parameters	
Surface tension, σ	0.0625 N/m
Contact angle, θ	110°
Dynamic viscosity of liquid water	3.5×10^{-4} Pa s
Dynamic viscosity of air	2.0×10^{-5} Pa s

For simplicity, Hagen–Poiseuille law originally derived for circular tubes is used to represent the flow through a throat, although Patzek and Silin [25] analytically derived a generalized Poiseuille law to represent flow in a throat of square cross-section and showed that the conductance of a square throat is 20% lower. No substantial differences are expected as the pressure drop across a throat does not govern the transport at small capillary numbers typically encountered in a PEFC operation.

In an invaded pore or throat, the wetting phase (air for hydrophobic GDL) can always be present along the corners in the form of wetting films [26]. The wetting films span through the network and provide connectivity to the wetting phase, thereby eliminating the possibility of wetting phase trapping in the porous medium. However, formation of wetting films along the corners is governed by the Concus and Finn [27] condition:

$$\theta + \gamma < 90^\circ \tag{3}$$

where θ and γ are contact angle between wetting phase and solid matrix and half corner angle of a pore or a throat, respectively. Thus, a contact angle between liquid water (non-wetting phase for hydrophobic GDL) and carbon fibers of 110° and square cross-section of pores and throats suppress the existence of wetting films along the corners. It should be mentioned that a small fraction of pores, having corner half angle less than 20°, in the actual pore spaces of carbon paper may allow simultaneous occupancy of a throat with both fluids. Incorporation of wetting film flow, in accordance with the Concus and Finn condition [27], in a topologically equivalent pore-network structure of carbon paper is envisioned as a future extension of the present PN model.

Table 2
Comparison of pore-network structure parameters with Toray® carbon paper

Parameter	Pore-network model	Toray® carbon paper
Mean pore diameter	20 μm	16–25 μm [35]
Thickness	250 μm	110–370 μm
Porosity	62%	78–80% (without PTFE loading) [36]
Absolute permeability (thickness direction)	5.6 Darcy	5–10 Darcy [35]
Absolute permeability (in-plane direction)	6 Darcy	5–12 Darcy [35]
Anisotropy factor (in-plane/through-plane)	1.07	1.3 (uncompressed) [24]

3.3. Two-phase flow algorithms

In the present work, a dynamic pore-network algorithm is deployed to study the dynamics of liquid water transport in a GDL that is initially saturated with air and is in contact with a liquid water reservoir at the inlet face. Some fraction of the outlet face of the GDL is masked by land regions; thereby liquid water can exit only through the gas channel portion. A 1:1 channel to land width ratio is used for the present study. The present dynamic model is used with a constant injection rate boundary condition at the inlet face to mimic the water production from a fuel cell catalyst layer, whereas constant pressure is applied at the outlet face.

For liquid water to invade a throat, the pressure difference across a meniscus must exceed the throat entry capillary pressure, given by Young–Laplace equation:

$$P_w - P_{air} > P_c, \quad P_c = \frac{2\sigma\cos\theta}{r_{th}} \tag{4}$$

where P_w and P_{air} represents liquid water and air pressure, respectively, P_c the capillary pressure and r_{th} is the throat radius. As is clear from Eq. (4), once a throat is invaded the connecting pore will be automatically invaded by liquid water owing to its larger size. Each phase, then, must obey volume conservation

within each pore body:

$$V_i \frac{\partial S_i^\alpha}{\partial t} + \sum_{j \in N_i} Q_{ij}^\alpha = 0, \quad i = 1, 2 \ldots N \tag{5}$$

where S_i^α is the local saturation of the phase α in pore i, N the total number of pores, V_i the volume of pore i, N_i the number of pores connected to pore i, and Q_{ij}^α is the flow rate of phase α between pore i and pore j. The flow rate of liquid water through a throat depends on the fluid configuration in the pores connected to that throat. For a liquid water-filled throat, connecting pores containing liquid water and air, the volumetric flow rate is given by

$$Q_{ij}^{\mathrm{w}} = \begin{cases} g_{\mathrm{w}}(P_i - P_j - P_{\mathrm{c}}) & \text{if } (P_i - P_j - P_{\mathrm{c}}) > 0 \\ 0 & \text{otherwise} \end{cases} \tag{6}$$

Physically, Eq. (6) means that flow through a throat is possible only if the pressure difference across the throat is higher than the throat entry capillary pressure, P_{c}. If pressure difference across a throat is less than the entry capillary pressure of the throat, it is called "capillary blocked" and flow cannot occur through that throat. Whereas for liquid water filled throat, connecting two liquid water-filled pores, the volumetric flow rate is given by

$$Q_{ij}^{\mathrm{w}} = g_{\mathrm{w}}(P_i - P_j) \quad \text{where } g_{\mathrm{w}} = \frac{2r_{\mathrm{th}}(i,\, j)^4}{\pi\, \mu_{\mathrm{w}} l(i,\, j)} \tag{7}$$

The constant injection rate at the inlet face is imposed by the following equation:

$$\sum_{\text{inlet pores}} [g_{\mathrm{w}}(P_i - P_{i+1} - P_{\mathrm{c}})] = Q_{\mathrm{in}} \tag{8}$$

The pressure field at every time step can be found by solving Eqs. (6)–(8). Once the pressure field is obtained, time steps are chosen so that only one pore reaches 100% liquid water saturation during any time step. Such a selection criterion of time step is in coherence with invasion percolation phenomena [28]. Using the value of current time step liquid water saturation is updated in all the pores. The pores filled with liquid water are then tested for instability of liquid water–air interface, using the most recent pressure field. If the pressure drop across an interface is larger than the corresponding throat entry capillary pressure, the interface is called "unstable", liquid water occupies the throat and the throat conductivity is updated accordingly. At any time step, volume averaged liquid water saturation, S^{w}, can be calculated as:

$$S^{\mathrm{w}} = \frac{\sum_{i \in \mathrm{RV}} V_i S_i^{\mathrm{w}}}{\sum_{i \in \mathrm{RV}} V_i} \tag{9}$$

where RV denotes the representative volume over which averaging is done. Eq. (9) can be used to obtain both cross-sectional averaged and overall liquid water saturation. As mentioned in the previous section, the liquid water transport in a GDL occurs at very low capillary number and thus requires near zero pressure gradient in the invading (liquid water) and defending (air) phases. The numerical framework to calculate pressure requires a "source" term at the inlet pores and a "sink", i.e. a throat having a non-zero conductance for liquid water flow, at each time step. Such a dynamic model may run into numerical difficulties if all the interfaces are capillary blocked at a particular time step. In order to avoid this situation, a "pseudo-percolation algorithm" proposed by Singh and Mohanty [29] is also included in the present study. If at a particular time step it is found that all the interfaces are capillary blocked, the throat having the least entry capillary pressure is made "open" for liquid water flow and the throat conductivity is updated accordingly. Physically, this corresponds to a sudden buildup of pressure at the inlet face and opening up of a throat for liquid water to drain in order to maintain a constant injection rate. Extended Hoshen–Kopelman algorithm [30] is used to determine air-trapped clusters at every time step. Trapped pores are excluded from the further calculation domain. This algorithm is run till the steady state is obtained.

3.4. Initial and boundary conditions

The GDL is initially saturated with air and the inlet face is in contact with a liquid water reservoir. In order to study the liquid water transport, a constant injection rate of liquid water is imposed on the inlet face, equivalent to 2.0 A cm^{-2} current density under the assumption that all the water produced is in liquid form. A constant pressure boundary condition is imposed on the outlet face, whereas all other faces are subjected to no-flow boundary condition.

4. Results and discussion

In a real fuel cell operation, liquid water appears on the GDL–channel interface in the form of droplets, which are carried away by the gas flow in channels [31,32]. Zhang et al. [32] investigated the effects of gas flow rate on cell performance and GDL–channel interfacial droplet dynamics and showed the existence of substantial amount of liquid water at the GDL–channel interface incurring mass transport losses at low gas flow rate. Hence it is essential to incorporate the appropriate GDL–channel interfacial condition in delineating flooding dynamics in a GDL. In the present work, liquid water transport is investigated first with zero GDL–channel surface coverage that corresponds to exceedingly high gas flow rates in the channel, after which the effect of GDL–channel interfacial coverage with liquid water on flooding dynamics is delineated.

4.1. Zero surface coverage

Physical insight can be gained from numerical visualization of liquid waterfront movement within the network during drainage, as depicted in Fig. 3, where irregular fractal patterns typical of invasion percolation are observed. It is clear from Fig. 3 that liquid water moves in the GDL through several continuous clusters. As liquid water invades the GDL, the liquid waterfront encounters multiple dead ends. The pressure difference across a gas–liquid interface must be larger than the capillary pressure at the interface for liquid water to invade

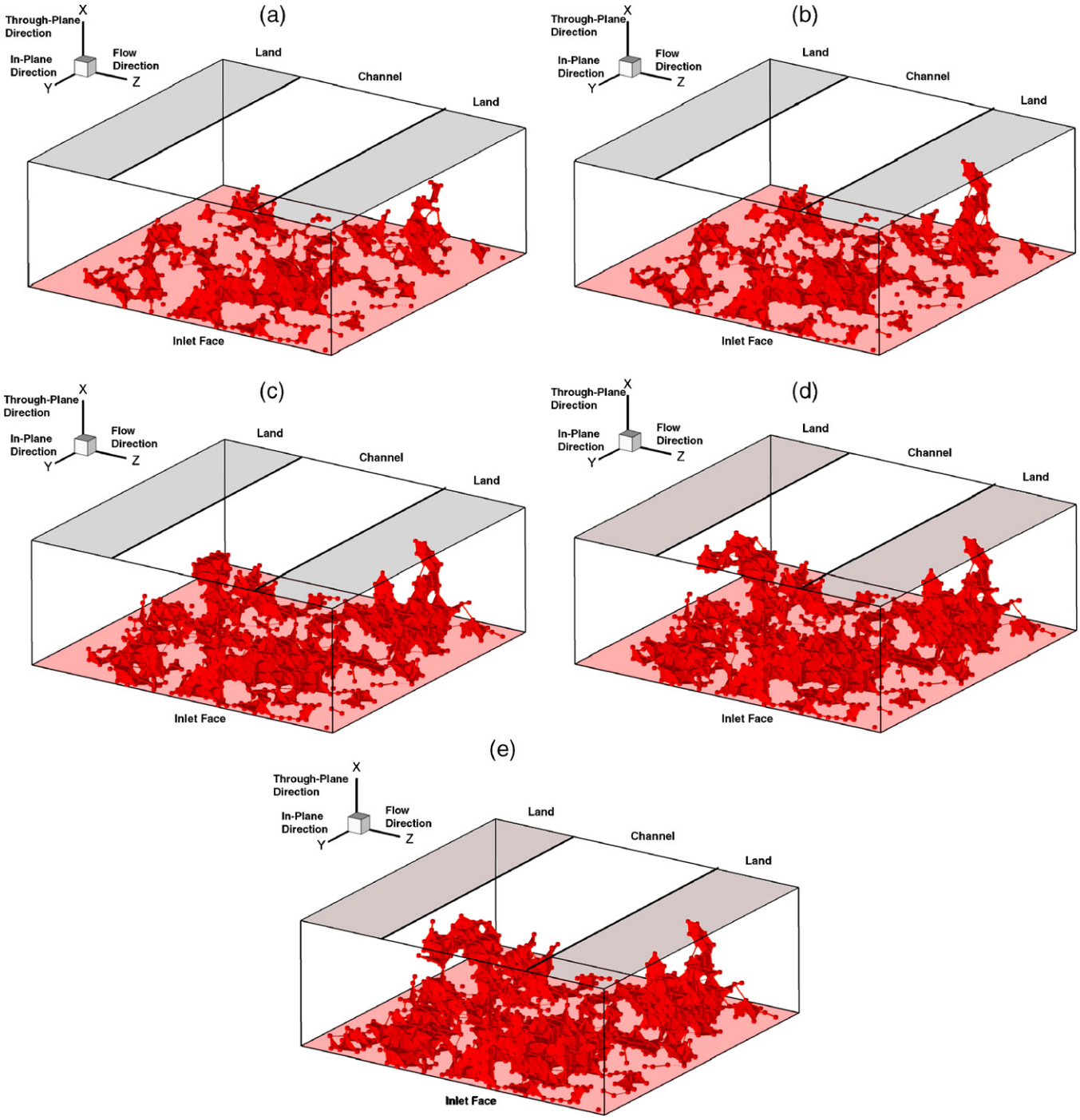

Fig. 3. Liquid waterfront movement in GDL with zero surface coverage: (a)–(d) at intermediate states, showing the evolution of capillary fingers and (e) at steady state.

further. Dead ends to front propagation appear when a liquid waterfront reaches a very narrow region with a very large entry capillary pressure. When a liquid waterfront encounters such a narrow region, the liquid water pressure increase at the inlet face makes the waterfronts unstable at several other locations and liquid water invades further into the GDL there. This mechanism can be more clearly explained with Fig. 4, where only "open clusters" during the liquid water transport in the GDL are displayed. The open clusters are defined as the liquid water clusters having non-zero flow rate at any instant of time. Fig. 4(a) shows the open clusters at an intermediate time step; but as liquid water invades further into the GDL, these liquid water clusters encounter dead ends and pressure at the inlet face increases to facilitate liquid water to flow through other clusters in order to maintain a constant flow rate, as shown in Fig. 4(b) and (c). Fig. 5 depicts the inlet pressure variation as a function of time. As shown in Fig. 5, pressure exhibits sudden jumps that physically correspond to sudden buildup of pressure at the inlet face causing irreversible burst, also known as "Haines Jump", of the liquid waterfront and then the inlet pressure adjusts itself to maintain

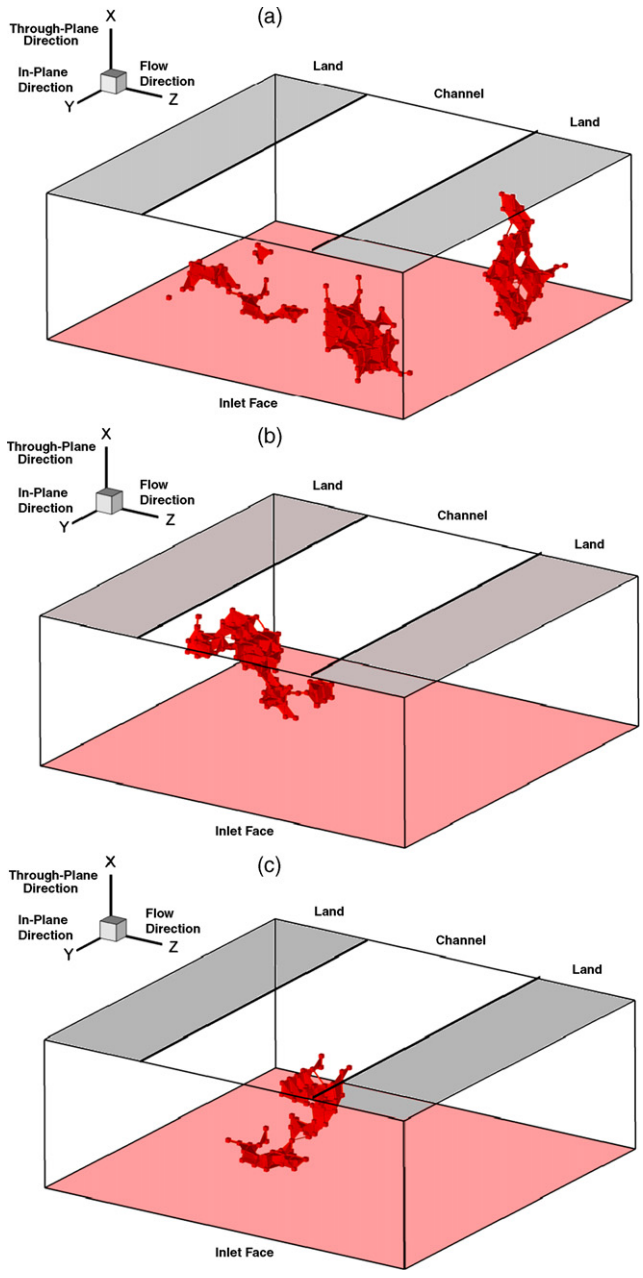

Fig. 4. Open liquid water clusters during liquid water transport in GDL with zero surface coverage: (a) and (b) at intermediate states and (c) at steady state.

the constant flow. As mentioned earlier, capillary number for liquid water movement in a GDL under realistic operating conditions is $\sim 10^{-8}$. Capillary forces thus control the transport of liquid water in GDL, entailing occupation of large pores with liquid water for any given pore-size distribution and uniform wettability. Therefore, several liquid clusters emanate from the inlet face according to the pore-size distribution of GDL with no directional dependence. This provides significant in-plane spreading of liquid clusters, especially near the inlet face of GDL, as shown in Fig. 3. This somewhat isotropic transport mechanism is in contrast with the Litster et al. [6] hypothesis of liquid water transport being dominated by through-plane fingering with little in-plane spreading. Substantial in-plane

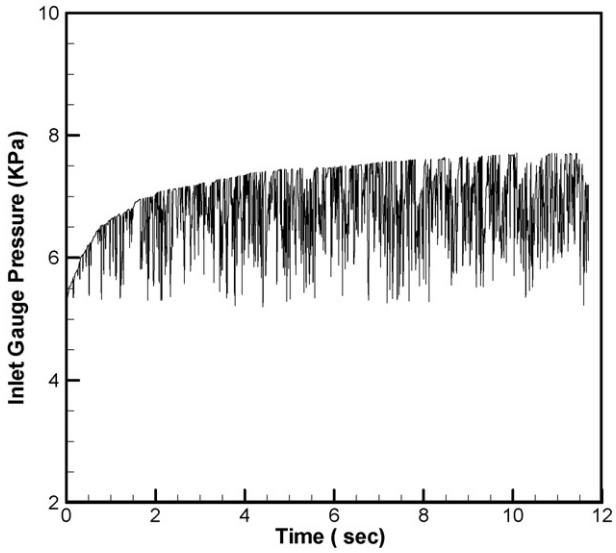

Fig. 5. Time-variation of inlet pressure during liquid water invasion in GDL with zero surface coverage.

spreading near the bottom of the GDL could explain the experimental observation that GDL flooding results in mass transport losses by blocking reactant transport through it, whereas minimal in-plane spreading of liquid water would imply negligible blocking of reactant transport and hence minimal mass transport losses.

Fig. 6 shows the evolution of the cross-sectional averaged liquid water saturation profile along the GDL thickness during water invasion. The saturation profiles observed in Fig. 6 are characteristic of fractal fingering flow. The occurrence of dead ends to multiple water clusters originating from the inlet face and the advancement of very few clusters following the paths of least resistance at low *Ca* result in a concave-shaped steady-state saturation profile. In comparison, two-phase PEFC

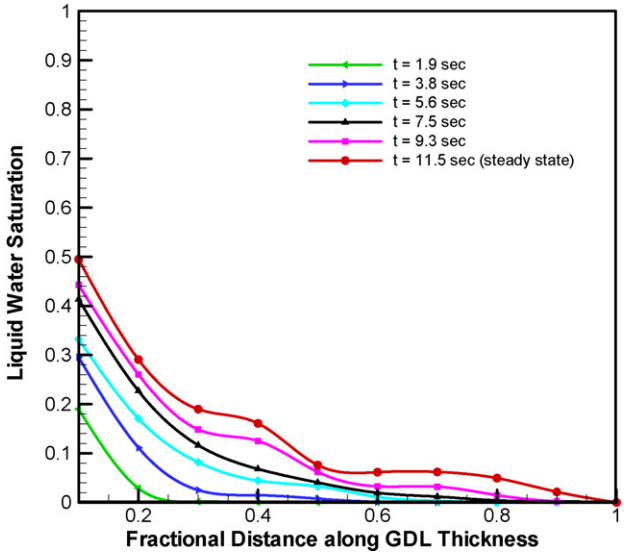

Fig. 6. Evolution of liquid water saturation profiles along the GDL thickness for zero surface coverage.

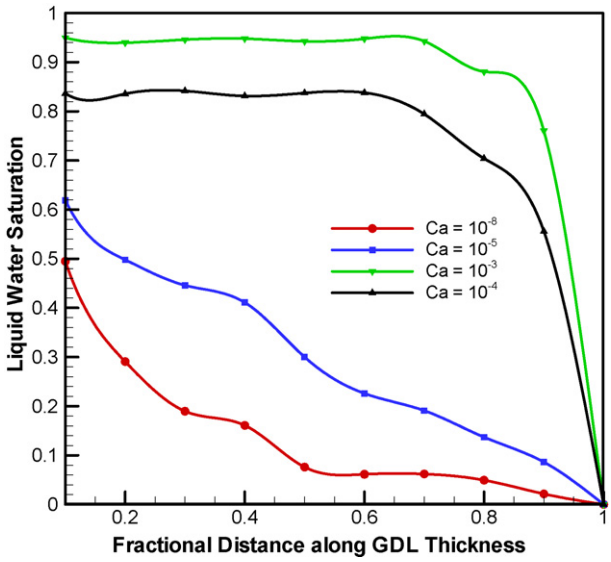

Fig. 7. Steady state liquid water saturation profiles along the GDL thickness as function of capillary number, *Ca*, for zero surface coverage.

macroscopic models published in the literature invariably yield convex-shaped saturation profiles, which are characteristic of stable displacement. It is expected that with increase in *Ca*, the fractal capillary fingering observed at low *Ca* crosses over to stable displacement, also known as compact invasion that can be predicted by Darcy's law based on saturation dependent relative permeabilities. To confirm the crossover from fractal capillary fingering to compact invasion, liquid water transport at different capillary numbers has been investigated. Fig. 7 shows the steady-state liquid water saturation profiles for capillary number varying from 10^{-8} to 10^{-3} (by increasing the flow rate). As can be seen, the characteristics of the saturation profile indeed change from a fractal form ($Ca = 10^{-8}$) to a stable flow form ($Ca = 10^{-4}$ and 10^{-3}) with increase in capillary number. This crossover from capillary fingering to compact invasion during drainage has been experimentally observed and investigated in detail in other applications [21,22,33,34]. The crossover in the liquid flow regime shown in Fig. 7 further underpins the necessity to match the capillary number in any ex situ experiments with that in an operating PEFC in order to properly characterize liquid flow regime and saturation profile in a GDL.

Further research is underway to elucidate the effect of mixed wettability on liquid water transport mechanisms and to find out whether the concave liquid saturation profile characteristic of fractal fingering also prevails in a realistic fuel cell GDL with a wettability distribution.

4.2. Non-zero surface coverage

Liquid water droplets at the hydrophobic GDL–channel interface grow to a critical size and are removed from GDL surface either by drag force exerted by the gas flow or by capillary wicking onto the neighboring hydrophilic channel walls. Recently, Zhang et al. [32] predicted the droplet detachment diameter as a function of air velocity in the gas channel based on simple force balance on a droplet but a detailed understanding of droplet growth dynamics remains absent in the literature. As a first attempt, however, the effect of interfacial liquid coverage is simulated by imposing a constant capillary pressure at the locations of liquid water breakout at the GDL–channel interface. A constant outlet capillary pressure of 7.7 kPa is applied in the present work.

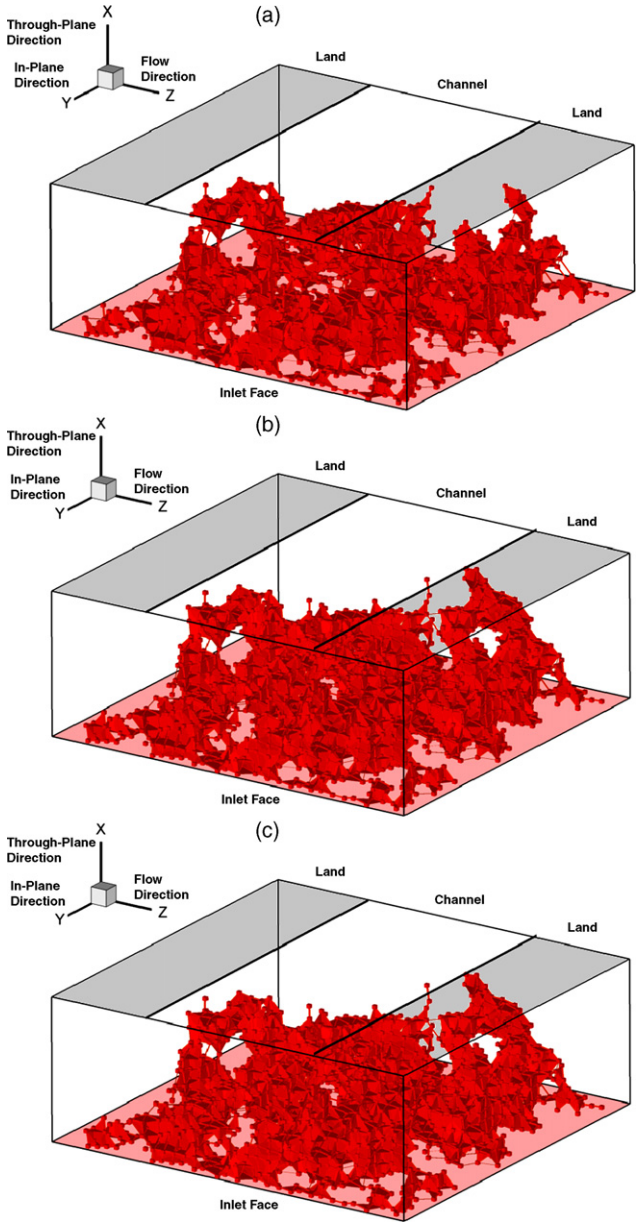

Fig. 8. Liquid waterfront movement in GDL with non-zero surface coverage: (a) at the break through of liquid water, (b) at an intermediate state and (c) at steady state.

Fig. 8 displays the liquid waterfront movement within the network. Fig. 8(a) shows the liquid water distribution when the first liquid water droplet appears at the outlet face and is very similar to the liquid water distribution for zero surface coverage at steady state, shown in Fig. 3(e). As soon as liquid water appears at an outlet location, liquid water pressure at the outlet increases and in order to maintain a constant flow rate, the inlet

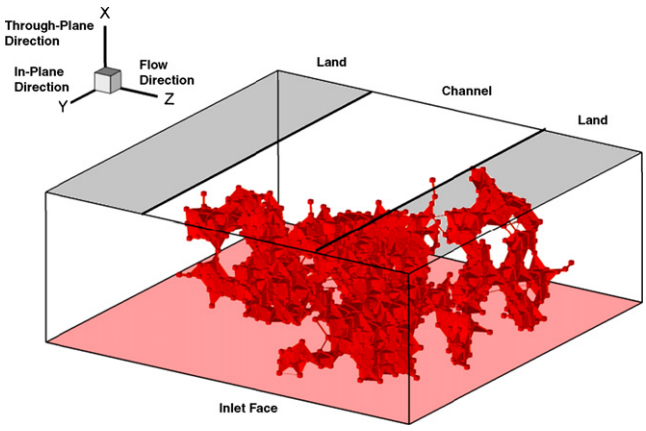

Fig. 9. Open liquid clusters at the steady state during liquid water transport in GDL with non-zero surface coverage.

pressure increases accordingly. The increase in the liquid pressure at the inlet makes the liquid water interface unstable at other locations and several "closed" liquid clusters open up again as shown in Fig. 8(b) and (c). Fig. 8(c) depicts the liquid waterfront at the steady state and clearly shows significantly higher liquid saturation as compared to the zero surface coverage case. Fig. 9 shows steady state open liquid clusters for non-zero surface coverage. As shown in Fig. 9, several clusters coalesce which were otherwise closed in the zero surface coverage situation, shown in Fig. 4(c). The breakout of liquid water from preferential locations is consistent with the experimental observations of Wang and co-workers [31,32]. Fig. 10 depicts the evolution of the cross-sectional averaged liquid water saturation profile along the GDL thickness. As shown in Fig. 10, GDL–channel interfacial surface coverage significantly increases the liquid water saturation inside the GDL and thus increases the mass transport losses to PEFC operation.

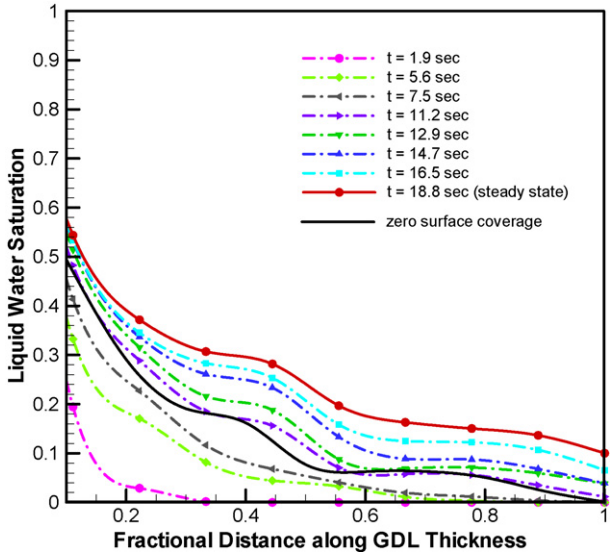

Fig. 10. Evolution of liquid water saturation profiles along the GDL thickness for non-zero surface coverage. Steady state saturation profile for zero surface coverage is shown for comparison.

5. Conclusions

A fundamental understanding of liquid water transport at pore-level addressing the roles of GDL morphology and wetting properties is essential to paint a clear picture of how flooding occurs and to determine the controlling factors. In the present work, a pore-network model describing governing physics of liquid water transport in a GDL at the pore-level is developed for the first time. It is seen that at extremely low capillary numbers as encountered in the fuel cell application, liquid water transport in a homogeneously hydrophobic GDL is governed by fractal capillary fingering. Liquid water flows through GDL in the form of connected clusters, encounters several dead ends due to the presence of narrow regions, and eventually percolates through a path of least resistance. The resulting saturation distribution of fractal capillary fingering cannot be described by two-phase Darcy's law that is applicable only for compact invasion at much higher capillary numbers ($Ca > 10^{-4}$ that is equivalent to 10^4 A cm^{-2} current density). Therefore, extensive research efforts are required to extend the present macroscopic treatment to account for capillary fingering phenomena encountered in a realistic PEFC operation. It is further stressed that matching capillary number and viscosity ratio in ex situ experiments is key to preserve liquid water flow regimes in a GDL. Presence of liquid water droplets at the GDL–channel interface is found to significantly increase liquid water saturation inside the GDL and lead to liquid water breakout from preferential locations, in accordance with experimental observations.

The present work delineates the pore-level liquid water transport mechanism in a uniformly hydrophobic GDL. However, the wide range of wetting characteristics of carbon-based materials as well as possible anomaly in the PTFE treatment might render a fraction of the GDL pores hydrophilic. Efforts are currently underway to elucidate liquid water transport in a mixed-wet GDL and to further generate a topologically equivalent pore-network structure for real GDL materials.

Appendix A. List of symbols

Ca	capillary number
g_α	throat conductance for phase α (m^4 s kg^{-1})
$l_{i,j}$	length of throat connecting pores i and j (m)
L	distance between two adjacent pores (m)
M	viscosity ratio
N	total number of pores
N_i	total number of pores connected to pore i
P	pressure (Pa)
P_c	capillary pressure (Pa)
Q_α	volumetric flow rate of phase α (m^3 s^{-1})
r	radius of pore (m)
r_{th}	radius of throat (m)
RV	representative volume
S	cross-sectional averaged liquid water saturation
S^α	saturation of phase α
V_i	volume of pore i (m^3)

Greek letters

γ	half angle of a pore or throat corner
ε	porosity
θ	contact angle
μ	dynamic viscosity (Pa s)
σ	surface tension (N m^{-1})

Subscripts

air	air
in	inlet
nw	non-wetting phase
w	water
wet	wetting phase

Superscript

w	water

References

[1] C.Y. Wang, in: W. Lietsich, A. Lamm, H.A. Gasteiger (Eds.), Handbook of Fuel Cells—Fundamentals, Technology and Applications, vol. 3, John Wiley & Sons, Chicester, 2003 (Chapter 29, p. 337).
[2] C.Y. Wang, Chem. Rev. 104 (2004) 4727.
[3] A. Faghri, Z. Guo, Int. J. Heat Mass Transf. 48 (2005) 19.
[4] J.T. Gostick, M.W. Fowler, M.A. Ioannidis, M.D. Pritzer, Y.M. Volfkovich, A. Sakars, J. Power Sources 156 (2006) 375.
[5] H. Ju, G. Luo, C.Y. Wang, J. Electrochem. Soc. 154 (2007) B218.
[6] S. Litster, D. Sinton, N. Djilali, J. Power Sources 154 (2006) 95.
[7] A. Bazylak, D. Sinton, Z.S. Liu, N. Djilali, J. Power Sources 163 (2007) 784.
[8] C. Pan, Ph. D. Dissertation, University of North Carolina, Chapel Hill, North Carolina, 2003.
[9] I. Fatt, Trans. AIME 207 (1956) 144.
[10] I. Fatt, Trans. AIME 207 (1956) 160.
[11] I. Fatt, Trans. AIME 207 (1956) 164.
[12] M.J. Blunt, M.D. Jackson, M. Piri, P.H. Valvatne, Adv. Water Resour. 25 (2002) 1069.
[13] K.E. Thompson, AICHE J. 48 (2002) 1369.
[14] M.J. Blunt, SPE J. 2 (1997) 70.
[15] A. Al-Futaisi, T.W. Patzek, J. Contam. Hydrol. 74 (2004) 61.
[16] M.J. Blunt, P. King, Transp. Porous Media 6 (1991) 407.
[17] E. Aker, M.J. Måløy, A. Hansen, G.G. Batrouni, Transp. Porous Media 32 (1998) 163.
[18] Y.Le. Brey, M. Prat, Int. J. Heat Mass Transf. 42 (1999) 4207.
[19] J.H. Nam, M. Kaviany, Int. J. Heat Mass Transf. 46 (2003) 4595.
[20] V.P. Schulz, J. Becker, A. Wiegmann, P.P. Mukherjee, C.Y. Wang, J. Electrochem. Soc. 154 (2007) B419.
[21] R. Lenormand, E. Touboul, C. Zarcone, J. Fluid Mech. 189 (1998) 165.
[22] R. Lenormand, J. Phys. Condes. Matter 2 (1990) SA79.
[23] R.P. Ewing, B. Berkowitz, Adv. Water. Resour. 24 (2001) 309.
[24] J.T. Gostick, M.W. Fowler, M.D. Pritzker, M.A. Ioannidis, L.M. Behra, J. Power Sources 162 (2006) 228.
[25] T.W. Patzek, D.B. Silin, J. Colloid Int. Sci. 236 (2001) 295.
[26] M.A. Ioannidis, I. Chatzis, Chem. Eng. Sci. 48 (1993) 951.
[27] P. Concus, R. Finn, Appl. Math. Sci. 63 (1969) 292.
[28] D. Wilkinson, J.F. Willemsen, J. Phys. A: Math. Gen. 16 (1983) 3365.
[29] M. Singh, K. Mohanty, Chem. Eng. Sci. 58 (2003) 1.
[30] A. Al-Futaisi, T.W. Patzek, Physica A 321 (2003) 665.
[31] X.G. Yang, F.Y. Zhang, A. Lubawy, C.Y. Wang, Electrochem. Solid State Lett. 7 (2004) A408.
[32] F.Y. Zhang, X.G. Wang, C.Y. Wang, J. Electrochem. Soc. 153 (2006) A225.
[33] M. Ferer, G.S. Bromhal, D.H. Smith, Physica A 319 (2003) 11.
[34] M. Ferer, G.S. Bromhal, D.H. Smith, Phys. Rev. E 67 (2003) 051601.
[35] M.F. Mathias, J. Roth, J. Fleming, W. Lehnert, in: W. Lietsich, A. Lamm, H.A. Gasteiger (Eds.), Handbook of Fuel Cells—Fundamentals, Technology and Applications, vol. 3, John Wiley & Sons, Chicester, 2003.
[36] Toray Industries Inc., http://www.torayca.com/main2.html.